A&A 658, A38 (2022)
https://doi.org/10.1051/0004-6361/202142063

Astronomy & Astrophysics

K2 discovery of a circumsecondary disk transiting EPIC 220208795

L. van der Kamp[1], D. M. van Dam[1], M. A. Kenworthy[1], E. E. Mamajek[2,3], and G. Pojmański[4]

[1] Leiden Observatory, University of Leiden, PO Box 9513, 2300 RA Leiden, The Netherlands
e-mail: lvanderkamp@strw.leidenuniv.nl
[2] Jet Propulsion Laboratory, M/S 321-100, 4800 Oak Grove Drive, Pasadena, CA 91109, USA
[3] Department of Physics & Astronomy, University of Rochester, PO Box 270171, Rochester, NY 14627, USA
[4] Astronomical Observatory, University of Warsaw, Al. Ujazdowskie 4, 00-478 Warszawa, Poland

Received 22 August 2021 / Accepted 23 October 2021

ABSTRACT

Context. Observations of the star EPIC 220208795 (2MASS J01105556+0018507) reveal a single, deep and asymmetric eclipse, which we hypothesise is due to an eclipsing companion surrounded by a tilted and inclined opaque disk, similar to those seen around V928 Tau and EPIC 204376071.
Aims. We aim to derive physical parameters of the disk and orbital parameters for the companion around the primary star.
Methods. The modelling is carried out using a modified version of the `python` package `pyPplusS`, and optimisation is done using `emcee`. The period analysis makes use of photometry from ground-based surveys, where we performed a period folding search for other possible eclipses by the disk. Parameters obtained by the best model fits are used to obtain the parameter space of the orbital parameters, while the most likely period obtained is used to constrain these parameters.
Results. The best model has an opaque disk with a radius of $1.14 \pm 0.03\ R_\odot$, an impact parameter of $0.61 \pm 0.02\ R_\odot$, an inclination of $77.01° \pm 0.03°$, a tilt of $36.81° \pm 0.05°$, and a transverse velocity of $77.45 \pm 0.05\ \mathrm{km\,s^{-1}}$. The two most likely periods are ∼290 days and ∼236 days, corresponding to an eccentricity of ∼0.7, allowing us to make predictions for the epochs of the next eclipses. All models with tilted and inclined disks result in a minimum derived eccentricity of 0.3, which in combination with the two other known small transiting disk candidates V928 Tau and EPIC 204376071, suggest that there may be a common origin for their eccentric orbits.

Key words. eclipses – planets and satellites: rings – binaries: eclipsing

1. Introduction

Advances in high precision photometry has allowed astronomers to continuously monitor the apparent brightness of stars, and some of these stars exhibit deep and irregular eclipses in their apparent brightness over time. These patterns can come from intrinsic stellar variability (Joy 1945; Lanza et al. 2007; Olah et al. 2009; Handler 2013) or external objects transiting the star, ranging from exoplanets, to exocomets (Rappaport et al. 2018; Zieba et al. 2019), to material in and above circumstellar disks (Ansdell et al. 2019; Kennedy et al. 2020) or infalling material onto white dwarfs (Vanderburg et al. 2015; Gänsicke et al. 2019). Other light curves challenge an easy identification of the associated astrophysical processes - two notable cases are Boyajian's star (Boyajian et al. 2016) and HD 139139 (Rappaport et al. 2019a). Dust that is believed to come from material in the inner part of circumstellar disks can produce dips in the brightness of stars that are called 'dippers' of ∼10–50% (Ansdell et al. 2016, 2019; Alencar et al. 2010; Cody et al. 2014; Cody & Hillenbrand 2018). Circumstellar disks are a universal feature of star formation and also dictate the structure of the planetary system that can be formed by the material inside these disks (Williams & Cieza 2011). The formation of gas planets is thought to be through the accretion of material from circumstellar disks that subsequently passes through a circumplanetary disk. A tilted and inclined disk around a planet or substellar companion can cause a dip in stellar brightness inconsistent with a transiting exoplanet eclipse. The projection of such a disk creates an elliptical occulting region and (for non-zero impact parameters) creates an asymmetric eclipse.

Analysing such systems can yield insights into the formation mechanisms of planets, especially if the observed system is young, since planets form and grow within protoplanetary disks. The properties and dynamics of these disks are connected, not only to stellar evolution and the evolution of a circumstellar disk, but also to the properties and evolution of the planet (Armitage 2011; Kley & Nelson 2012). Analysing a transit can reveal the structure of the circumplanetary disk and provide insight into the dynamics and mechanics of ring and moon formation (Teachey et al. 2017). Examples of disk systems or dusty occultations analysed in previous studies are 'J1407' (V1400 Cen, Kenworthy & Mamajek 2015), EPIC 204376071 (EPIC 2043, Rappaport et al. 2019b), and V928 Tau (van Dam et al. 2020). In the case of J1407, a ring system is hypothesised to be around a secondary companion occulting the star, whereas the other two systems are of an inclined circular disk around a secondary companion occulting the star. An elliptical occulter has recently been suggested for the light curve seen towards the late type giant star labelled VVV-WIT-08 (Smith et al. 2021) discovered as part of the VISTA Variables in the Via-Lactea (VVV; Minniti et al. 2010; Minniti et al. 2017) survey, although this is closer in diameter to the J1407 occulter, and it produced an eclipse that lasted about 200 days.

The *Kepler* mission was launched to determine the frequency of Earth-sized planets in and near the habitable zone of Sun-like stars (Borucki et al. 2010). The mission has

measured a large number of high-resolution light curves and has discovered a great deal of exoplanets (Thompson et al. 2018). After the failure of *Kepler*'s second reaction wheel in May 2013, the repurposed K2 mission (Howell et al. 2014) was able to survey the ecliptic plane, leading to numerous additional discoveries (Mayo et al. 2018). Several single, deep transit events have been identified in the K2 data (LaCourse & Jacobs 2018), and we examine the curves that have been classified as 'Deep', looking specifically for asymmetric eclipses as these hint at an elliptical occulter. EPIC 220208795 (EPIC 2202), also known by the aliases TIC 336889445, 2MASS J01105556+0018507, SDSS J011055.57 +001850.6, and *Gaia* DR2 2534801707104852864, shows a deep and asymmetric transit event similar to the ones observed in Rappaport et al. (2019b); van Dam et al. (2020) and we model this eclipse with a tilted and inclined disk around a companion occulting the star. Section 2 gives a description of the telescopes and the photometry obtained from them, and the preliminary analysis on the K2 light curves to identify the most likely candidates for a tilted and inclined disk transit and why we proceeded with EPIC 2202. Section 3 describes the modelling of the asymmetric dip found in the EPIC 2202 light curve and we give a description of the best fits for two separate models. In Sect. 3.5 we perform a period folding analysis using ground-based survey photometry to determine the most likely period given the photometry available and identify other possible eclipses. Section 3.6 contains the orbital analysis of the best fit models, obtaining orbital parameters like the eccentricity and periastron distance. In Sect. 4 we discuss our results, point out limitations of our modelling, and compare them to two other disk systems from Rappaport et al. (2019b) and van Dam et al. (2020). Section 5 summarises our findings and presents suggestions for future research.

2. Data

The entire code used for the analysis and creating the figures in this paper is available online[1].

2.1. K2

The *Kepler* spacecraft is a 0.95 m Schmidt telescope with a 1.4 m diameter primary and a 110 deg^2 field of view. The prime focus camera has 42 CCDs that are 2200×1024 pixels (Borucki et al. 2010). The extended K2 mission observed EPIC 2202 during campaign 8 (2016-Jan-03 to 2016-Mar-23) for a total of 79 days. It collected 3840 observations, with a cadence of 30 minutes, in the K_p filter, with a bandpass of 420–900 nm. Further information is listed in Table 1.

The light curve was extracted using `EVEREST 2.0`, (Luger et al. 2016, 2018), which is an open-source pipeline for removing instrumental noise from K2 data. It uses a variant of Pixel Level Decorrelation (PLD; Deming et al. 2015) to reduce systematic errors caused by the *Kepler* spacecraft's pointing error, such as the 6 h trend in the raw aperture photometry, which compromises its ability to detect small transits. The light curve reveals a star with low amplitude flux variations (less than 1%), which were deemed small enough to avoid stellar variability modelling.

Although the main science mission for *Kepler* and K2 was the detection and characterisation of exoplanet transits, the library of light curves collected include many other types of astrophysical phenomena. To this end, LaCourse & Jacobs (2018) manually inspected 238 399 stellar light curves and identified 48 stars that showed deep or unusual eclipses. Ten stars were observed on two separate campaigns resulting in a total of 53 light curves. The light curves were examined for asymmetry as this is a tell-tale sign of an elliptical occulter, which hints at circumsecondary disk transits. Of these targets we determined that EPIC 2202 was the most likely candidate for a tilted and inclined disk system, similar to the transits seen in the case of EPIC 2043 and V928 Tau. The eclipse of EPIC 2202 lasts for about 7.2 h with a maximum depth of about 25% (see Fig. 1).

2.2. TESS

The Transiting Exoplanet Survey Satellite (TESS) is a satellite designed to survey for transiting exoplanets among the brightest (and nearest) stars over most of the sky (Ricker et al. 2015). The TESS satellite orbits the Earth every 13.7 days on a highly elliptical orbit, scanning a sector of the sky spanning 24×96 deg^2 for a total of two orbits, before moving on to the next sector. It captures images at a 2 s (used for guiding), 20 s (for 1 000 bright asteroseismology targets), 120 s (for 200 000 stars that are likely planet hosts) and 30 min (full frame images) cadences. The instrument consists of 4 CCDs each with a field of view of 24×24 deg^2, with a wide band-pass filter from 600–1000 nm (similar to the I_C band) and has a limiting magnitude of about 14–15 mag (I_C). Further information is presented in Table 1.

EPIC 2202 was observed in Sector 3 (2018-Sep.-20 to 2018-Oct.-18) providing 770 photometric points with a cadence of 30 minutes and in Sector 30 (2020-Sep.-22 to 2020-Oct.-21) providing 3511 photometric points with a cadence of 10 min (see Fig. 2). Photometry for TESS has been processed using the `eleanor` (Feinstein et al. 2019), an open-source tool that produces light curves from TESS Full Frame Images.

2.3. Ground-based surveys

To supplement the space-based data obtained by K2 and TESS, several archival databases for ground-based surveys were queried for data on EPIC 2202, resulting in three sets of light curves. This relatively low number is most likely due to the fact that EPIC 2202 is faint (see Table 2).

The first of these ground-based surveys is the All Sky Automated Survey (ASAS; Pojmanski 1997, 2005; Simon et al. 2018). This is a survey consisting of two observing stations - one in Las Campanas, Chile, and the other on Maui, Hawaii. Recently each observatory was equipped with two CCD cameras using V and I filters and commercial f = 200 mm, D = 100 mm lenses, although earlier both larger (D = 250 mm) and smaller (50–72 mm) lenses were used. Most data are taken with pixel scale of $\approx 15''$. ASAS splits the sky into 709 partially overlapping (9×9 deg^2 fields, taking on average 150 3-min exposures per night, leading to variable cadence of 0.3–2 frames per night. Depending on the equipment used and the mode of operation, the ASAS limiting magnitude varied between 13.5 and 15.5 mag in V, and the saturation limit was 5.5–7.5 mag. Precision is around 0.01–0.02 mag for bright stars and below 0.3 mag for the faint ones. ASAS photometry is calibrated against the Tycho catalogue, and its accuracy is not better than 0.05 mag for bright, non-blended stars.

The second is the All Sky Automated Survey for Supernovae (ASAS-SN; Shappee et al. 2014; Kochanek et al. 2017) which consists of six stations around the globe, with each station hosting four telescopes with a shared mount. The telescopes consist of a 14-cm aperture telephoto lens with a field of view of approximately 4.5×4.5 deg^2 and an $8.0''$ pixel scale. Two of

[1] https://github.com/lizvdkamp/EPIC2202_disk

Table 1. Overview of the time-series photometric instruments.

Survey	Filter	$n_{\rm tel}$	$n_{\rm phot}$	Baseline (days)	Start date	End date	Field of view (deg^2 cam^{-1})	Pixel-scale ($''$ pix^{-1})
ASAS [(a)]	I	1–4	85	2026	27-12-2002	14-07-2008	4.8, 77.4	14.2
	V		829	7007	20-11-2000	27-01-2020		
ASAS-SN	g	12	1604	1244	17-09-2017	12-02-2021	4.5	8.0
	V	8	1049	2371	02-06-2012	29-11-2018		
ATLAS	c	2	356	2006	12-08-2015	07-02-2021	29.2	1.9
	o		892	1926	23-10-2015	01-02-2021		
K2	K_p	1	3840	79	04-01-2016	23-03-2016	110	4.0
TESS	$I_C^{(b)}$	1	770	20	24-09-2018	14-10-2018	576	21

Notes. [(a)]In 2000 the survey upgraded to two telescopes in Chile. In 2006 two telescopes in Hawaii were added. [(b)]Centred on the traditional I_C band, but has a 600–1000 nm bandpass.

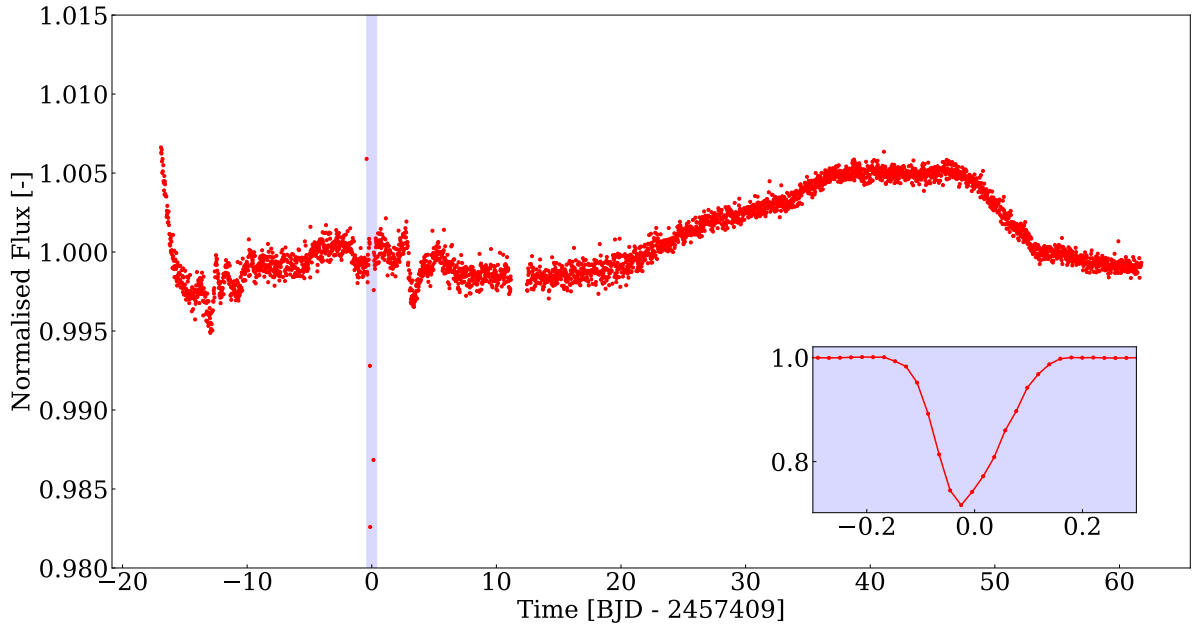

Fig. 1. `EVEREST 2.0` light curve of EPIC 2202 with the eclipse centred at BJD 2457409, highlighted in pale blue. Points with non-zero `QUALITY` values are removed, and the eclipse points have been added back into the light curve (these were incorrectly removed in the pipeline).

the original stations (one in Hawaii and one in Chile) are fitted with V band filters, whereas the additional stations (Chile, Texas, South Africa, and China) are fitted with g band filters. ASAS-SN observes the whole sky every night with a limiting magnitude of about 17 mag in the V and g bands. The data was obtained through the publicly available Sky Patrol Service[2].

The third and final survey is the Asteroid Terrestrial-impact Last Alert System (ATLAS; Heinze et al. 2018; Tonry et al. 2018). This is a deep survey with a limiting magnitude of 19 and a precision of around 0.01–0.04 mag. It consists of two telescopes in Hawaii with a 0.65 m primary mirror and a 0.5 m Schmidt corrector. Mounted on the telescope is a camera with a 13.5-cm aperture lens, which when combined with the main telescope, provides a field of view of approximately 29 deg^2. The ATLAS survey uses three special filters c (cyan, 420–650 nm), o (orange, 560–820 nm) and t (tomato, 560–975 nm), that are designed to be differentially sensitive to the silicate colours of stony asteroids. Data for the ATLAS survey was obtained via their online 'forced photometry' server[3].

Further information on the ground-based surveys is presented in Table 1 and a light curve of all the photometric time-series data collected is presented in Fig. 3.

2.4. Photometry and astrometric data

Table 2 summarises the available astrometry and photometry for EPIC 2202. The parallax and proper motion are listed from *Gaia* Early Data Release 3 (*Gaia* EDR3; Gaia Collaboration 2021), and the distance is a geometric estimate based on the *Gaia* EDR3 parallax taking into account a prior Galactic model (Bailer-Jones et al. 2021). Mean photometric magnitudes are provided by *Gaia* EDR3, the Two Micron All Sky Survey (2MASS; Skrutskie et al. 2006), and the Sloan Digital Sky Survey Data Release 8 (SDSS DR8; Aihara et al. 2011).

[2] https://asas-sn.osu.edu

[3] https://fallingstar-data.com/forcedphot/

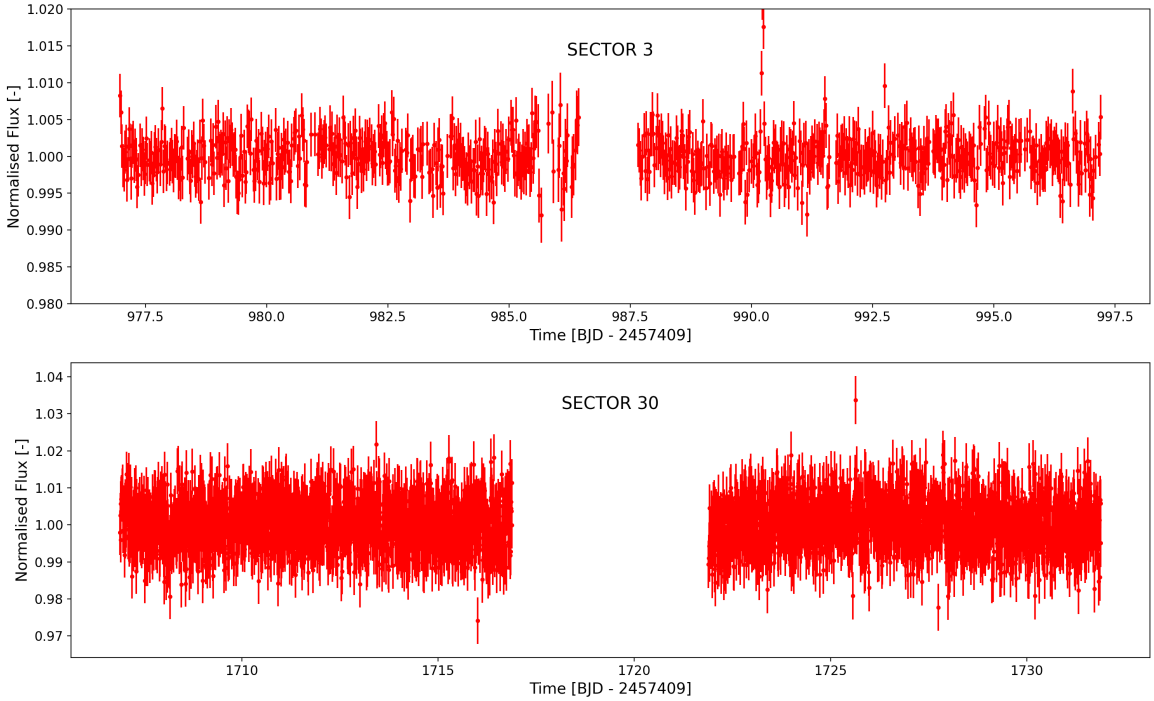

Fig. 2. `Eleanor` light curve of EPIC 2202. The *upper panel* shows Sector 3 and the *lower panel* shows Sector 30. We note that in Sector 30 there was significantly more scattered light, which explains the larger scatter and the larger absence of data between the two orbits.

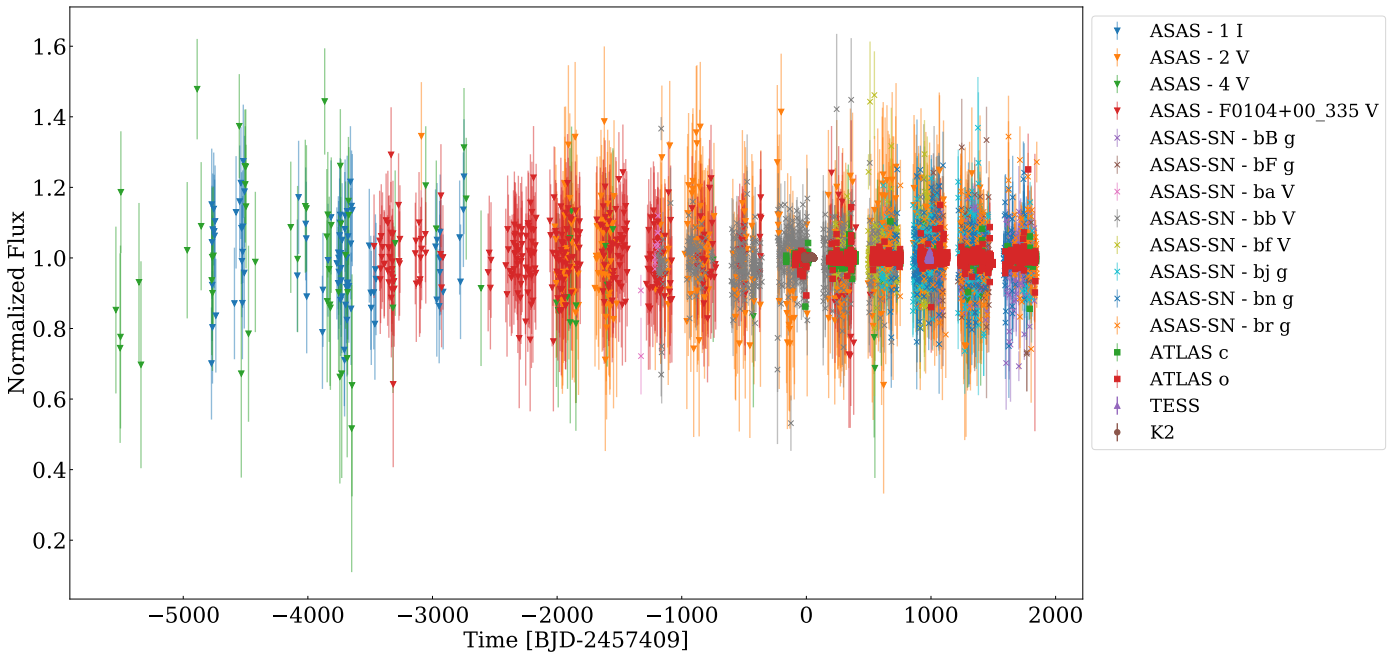

Fig. 3. Time-series photometry of EPIC 2202 from several ground-based surveys as well as the K2 and TESS data. Photometry with a flux value greater than 150% or less than 10% was excluded, along with flux errors error greater than 100%.

3. Analysis

3.1. Stellar parameters

To independently estimate basic stellar parameters for EPIC 2202, we use the Virtual Observatory SED Analyzer 6.0 (VOSA; Bayo et al. 2008)[4] to construct the star's Spectral Energy Distribution (SED) and fit synthetic stellar spectra. For reddening, we adopt the full Galactic dust column in the direction of the star from Schlafly & Finkbeiner (2011) ($E(B–V)$ = 0.0219 ± 0.0003) as the STILISM 3D reddening maps from Lallement et al. (2018) show that the dust in the direction of the star is mostly confined to within $d < 335$ pc and the star lies at a *Gaia* EDR3-inferred distance of $d = 487 \pm 6$ pc (Bailer-Jones et al. 2021). For dwarf stars of $T_{\rm eff} \simeq 5000$ K, a typical Galactic ratio of total to selection extinction value of $R_{\rm V}$ (=$A_{\rm V}/E(B–V)$) is 3.2 (McCall 2004), with $\sigma_{R_{\rm V}} \simeq 0.18$ so we adopt an interstellar

[4] http://svo2.cab.inta-csic.es/theory/vosa/

Table 2. Properties of EPIC 2202.

Property	Value	Ref.
$\alpha_{\rm ICRS}$, J2000 [hh mm ss]	01:10:55.573	1
$\delta_{\rm ICRS}$, J2000 [dd mm ss]	+00:18:50.52	1
μ_α [mas yr^{-1}]	14.642 ± 0.026	1
μ_δ [mas yr^{-1}]	−8.103 ± 0.019	1
ϖ [mas]	2.0152 ± 0.0230	1
Distance [pc]	$486.6^{+6.7}_{-5.9}$	2
G [mag]	14.2645 ± 0.0028	1
$G_{\rm BP}$ [mag]	14.7271 ± 0.0033	1
$G_{\rm RP}$ [mag]	13.6425 ± 0.0039	1
J [mag]	12.897 ± 0.026	3
H [mag]	12.431 ± 0.024	3
K_s [mag]	12.321 ± 0.024	3
u (AB) [mag]	17.63 ± 0.02	4
g (AB) [mag]	16.096 ± 0.008	4
r (AB) [mag]	16.69 ± 0.02	4
i (AB) [mag]	14.123 ± 0.005	4
z (AB) [mag]	14.832 ± 0.011	4
R_* [$R_\odot$]	0.830 ± 0.022	5
M_* [$M_\odot$]	0.85 ± 0.02	5
[Fe/H] [dex]	$+0.02^{+0.15}_{-0.14}$	6
$\log g$ [$\log_{10}$ cm s^{-2}]	$4.56^{+0.03}_{-0.05}$	6
$T_{\rm eff}$ [K]	5060 ± 50	5
$f_{\rm bol}$ [10^{-11} erg s^{-1}]	5.288 ± 0.130	5
$m_{\rm bol}$ [mag]	14.194 ± 0.027	5
$M_{\rm bol}$ [mag]	5.716 ± 0.036	5
$L_{\rm bol}$ [$L_\odot$]	0.4070 ± 0.0137	5
$\log(L/L_{\rm bol})$ [dex]	−0.3904 ± 0.0146	5

References. (1) *Gaia* EDR3 (Gaia Collaboration 2021), (2) Bailer-Jones et al. (2021), (3) 2MASS (Cutri et al. 2003), (4) SDSS DR8, (5) this work, (6) StarHorse (Anders et al. 2019).

extinction $A_V = 0.070$. Using the relation $A_{Ks} = 0.382\,E(B\text{-}V)$ from Bilir et al. (2008), we estimate the K_s extinction to be $A_{Ks} = 0.0084$. Photometry from several surveys was included in the SED fitting, incuding: GALEX NUV (Bianchi et al. 2011), Sloan DR9 *ugriz* (Adelman-McCarthy et al. 2011).

For the fits of the photometry to the synthetic stellar spectra (see Fig. 4), we constrained the extinction $A_V \in [0.06, 0.08]$, surface gravity $\log g \in [4, 5]$, and metallicity [M/H] ∈ [−0.5, 0.5], as the star is clearly a dwarf and the photometric metallicities are approximately solar with [M/H] = $+0.02^{+0.15}_{-0.14}$ (Anders et al. 2019). For a grid of Kurucz ATLAS9 models (Castelli & Kurucz 2003), the best fit spectral template (fitting 27 photometric bands) was $T_{\rm eff}$ = 5000 K, [M/H] = +0.5, $\log g$ = 4, $L = 0.407 \pm 0.010\,L_\odot$. Varying whether the UV photometry (GALEX NUV) or reddest IR bands (WISE *W3* and *W4*) were included or not, and examining the scatter in output parameters when varying metallicity, surface gravity, or extinction within the previous bounds, all had negligible effect on the resultant bolometric flux and luminosity. No ultraviolet (NUV) or infrared (for example, WISE *W3* and *W4*) excess was apparent. From this SED analysis we adopt the following parameters: bolometric flux $f_{\rm bol} = 5.288(\pm0.130) \times 10^{-11}$ erg s^{-1} cm^{-2}, apparent bolometric magnitude $m_{\rm bol} = 14.194 \pm 0.027$ (IAU 2015 scale), absolute bolometric magnitude $M_{\rm bol} = 5.716 \pm 0.036$ (IAU 2015 scale), bolometric luminosity $L = 0.4070 \pm 0.0137\,L_\odot$, and $\log(L/L_{\rm bol}) = -0.3904 \pm 0.0146$ dex.

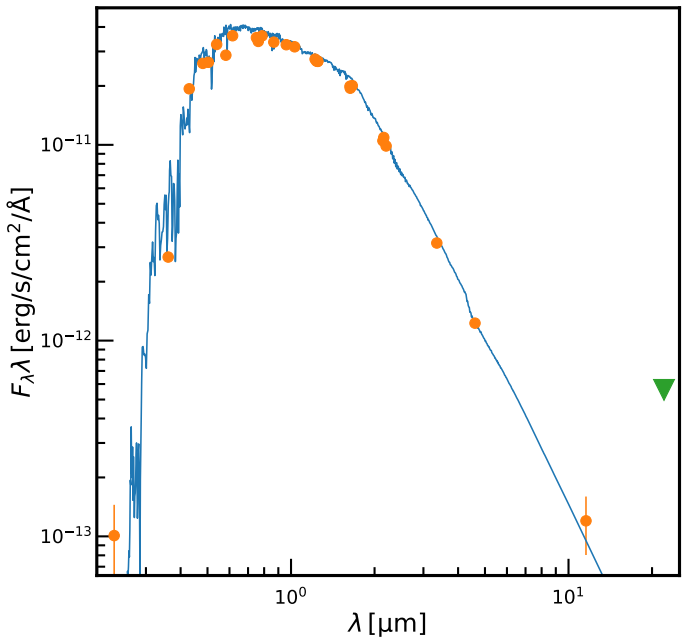

Fig. 4. Spectral energy distribution for EPIC 2202. The blue curve is a Kurucz best fit model. The orange points are the photometry as compiled from SIMBAD. The green triangle is an upper limit measurement from WISE at 22 microns.

Table 3. Estimated effective temperatures for EPIC 2202.

$T_{\rm eff}$ [K]	Reference
4997^{+97}_{-46}	Gaia Collaboration (2018)
5000	This work
5064^{+102}_{-81}	Huber et al. (2016)
5090 ± 46	Bai et al. (2019)
5095 ± 122	Stassun et al. (2019)
5105 ± 138	Hardegree-Ullman et al. (2020)
5206^{+156}_{-104}	Anders et al. (2019)
5060 ± 50	Adopted

There are several other published $T_{\rm eff}$ estimates for EPIC 2202, listed in Table 3. The $T_{\rm eff}$ estimates are in reasonable statistical agreement with one another. The Anders et al. (2019) value is somewhat high, likely due to adopting an excessive extinction (A_G = 0.20) which does not appear to be supported by the extinction maps (Schlafly & Finkbeiner 2011; Lallement et al. 2018). Omitting the Anders et al. (2019) value, we adopt the unweighed mean $T_{\rm eff}$ of the remaining values, and adopt the standard deviation as a conservative estimate of the uncertainty: $T_{\rm eff} = 5060 \pm 50$ K (1.0% uncertainty). This $T_{\rm eff}$ is typical for a solar composition K2V star (Pecaut & Mamajek 2013)[5]. Combining the adopted $T_{\rm eff}$ estimate with the previously estimated luminosity from our SED analysis, we estimate the radius of EPIC 2202 to be $R = 0.830 \pm 0.022\,R_\odot$ (IAU nominal solar radius) or 577 600 ± 15 100 km (2.6% uncertainty).

Only two mass estimates have been published since the availability of parallax data for EPIC 2202 by *Gaia* DR2. Anders et al. (2019) (StarHorse) estimates the mass to be $0.827^{+0.057}_{-0.031}$ $M_\odot$, and the TIC version 9 (Stassun et al. 2019) estimates the

[5] http://www.pas.rochester.edu/~emamajek/EEM_dwarf_UBVIJHK_colors_Teff.txt

mass to be 0.850 $M_\odot$ (no uncertainties). Huber et al. (2016) estimated the mass to be $0.816^{+0.050}_{-0.070}$ $M_\odot$, however this was without the benefit of a trigonmetric parallax. Using the most recent mass-luminosity calibration for binary stars with dynamical masses from Eker et al. (2018), our luminosity estimate ($\log(L/L_\odot)$ = -0.390) translates to a mass estimate of 0.858 $M_\odot$. Based on these three estimates (Stassun et al. 2019; Anders et al. 2019, and this work), we adopt a stellar mass of 0.85 ± 0.02 $M_\odot$.

3.2. Eclipse modelling

The eclipse observed in K2 photometry is most likely due to an occulter transiting EPIC 2202. The asymmetry and depth of the eclipse, as well as the short duration, make it unlikely for the transiting object to be a spherically symmetric object. We assume that the eclipse is due to a tilted and inclined disk gravitationally bound to an unseen secondary companion that creates an elliptical occulter due to its projected geometry. We model the light curve with two models – a hard edged disk, and a two ring disk consisting of an inner opaque disk and an outer, partially transmissive ring.

3.2.1. Model parameters

The modelling is performed using a modified version of the `pyPplusS` package that models the transit of an oblate exoplanet or an exoplanet with rings by calculating the area hidden by the occulter across the limb-darkened disk of the star (Rein & Ofir 2019). We use this to model the light curve based on the position and geometry of the disk with respect to the (limb-darkened) host star. The code works the spatial domain (in units of stellar radii) and must be converted to the temporal domain, by introducing a transverse velocity v_t and fitting for δt with respect to BJD = 2 457 409, to produce a light curve.

To calculate a lower bound on v_t we use the method described in van Werkhoven et al. (2014). This method requires the linear limb-darkening parameter, u, of the star, which has been determined using the `jkltd` programme written by Southworth (2015). This programme uses the surface gravity, $\log g$, the effective temperature, $T_{\rm eff}$, and the metallicity, [Fe/H], of the star to linearly interpolate the tables from Sing (2010) to calculate u for the *Kepler* bandpass. These values are derived by Huber et al. (2016) for 138 600 K2 targets in campaigns 1–8, using proper motions, colours, parallaxes, spectroscopy, and stellar population models. For EPIC 2202 we have $\log g$ = 4.591, $T_{\rm eff}$ = 5064 K, and [Fe/H] = −0.112, which results in a value of u = 0.6681.

Using u, the steepest time gradient of the light curve, $\dot{L}$, and taking $R = R_*$, we can get a lower limit on v_t following the method of van Werkhoven et al. (2014):

$$v_t = \dot{L} R \pi \left(\frac{2u - 6}{12 - 12u + 3\pi u} \right). \quad (1)$$

For our obtained value of u and for $\dot{L}$ = 3 L_* day^{-1} we obtain a lower limit of v_t = 4.3 R_* day^{-1}.

The free parameters for the model are the radius of the disk, $R_{\rm d}$, the impact parameter (perpendicular distance between the centre of the star and the orbital path), b, the inclination of the disk, i, the tilt of the disk (the angle with respect to the orbital path), ϕ, the transverse velocity of the disk, v_t, the time shift with respect to the time of closest approach, δt, and the opacity of the disk τ.

We use `emcee` (Foreman-Mackey et al. 2013) to explore these parameters and use Markov chain Monte Carlo (MCMC) methods to determine the best fit of the models. To properly explore this parameter space physical bounds on these parameters must be applied. These are as follows: an upper limit for $R_{\rm d}$ of ten times the radius of the star, R_*, the upper and lower limit on b are such that the disk must transit the star, the bounds on i are from 0° (face-on disk) to 90° (edge-on disk), ϕ has been limited from 0° to 90° because of reflection symmetries induced by the combination of b and ϕ, and a range of δt between −10 and 10 days. We take v_t between 4.3 R_* day^{-1} and 20 R_* day^{-1}, where the upper bound has been deemed large enough and the lower bound has been calculated above. The opacity of the disk, τ, can generally be bound between 0 and 1, but here we fix τ at 1, to get the smallest possible disk.

Table 4. Parameter bounds for MCMC optimisation.

Parameter	Lower bound	Upper bound
$R_{\rm d}$ [R_*]	0	10
$t_{\rm e}$ [R_*]	0	10
b [R_*]	−10	10
i [°]	0	90
ϕ [°]	0	90
v_t [R_* day^{-1}]	4.3	20
δt [day]	−10	10
τ [-]	1	1
$\tau_{\rm e}$ [-]	0	1

Table 5. Gaussian priors for MCMC optimisation.

Parameter	Hard edged disk		Soft edged disk	
	Median	Spread	Median	Spread
$R_{\rm d}$ [R_*]	0.9	0.1	1.4	0.1
$t_{\rm e}$ [R_*]	–	–	0.1	0.1
b [R_*]	0.3	0.1	0.7	0.1
i [°]	72	6	77	6
ϕ [°]	49	6	37	6
v_t [R_* day^{-1}]	10.0	0.5	11.6	0.1
δt [day]	–0.04	0.10	–0.04	0.01
τ [-]	–	–	–	–
$\tau_{\rm e}$ [-]	–	–	0.1	0.1

3.2.2. Hard edged disk

The first model we explore is a hard edged disk. We fix the opacity such that the disk is completely opaque, since this gives the smallest possible disk diameter for a given light curve gradient. The smallest physically plausible disk model then gives a lower bound on the mass of the secondary companion through the size of the companion's Hill sphere. We are interested in the smallest possible disks as these are deemed more likely to exist due to stability of the disk, and orbital velocity considerations.

To determine a suitable starting point of the fit we set a Gaussian prior bound by the limits in Table 4 and described in the previous section. We ran this for 600 links with 1000 walkers. We used a local minimum from this parameter investigation to set the initial starting point for the walkers of the extended optimisation. This starting point was expanded with Gaussian priors to produce the initial parameter spread summarised in Table 5.

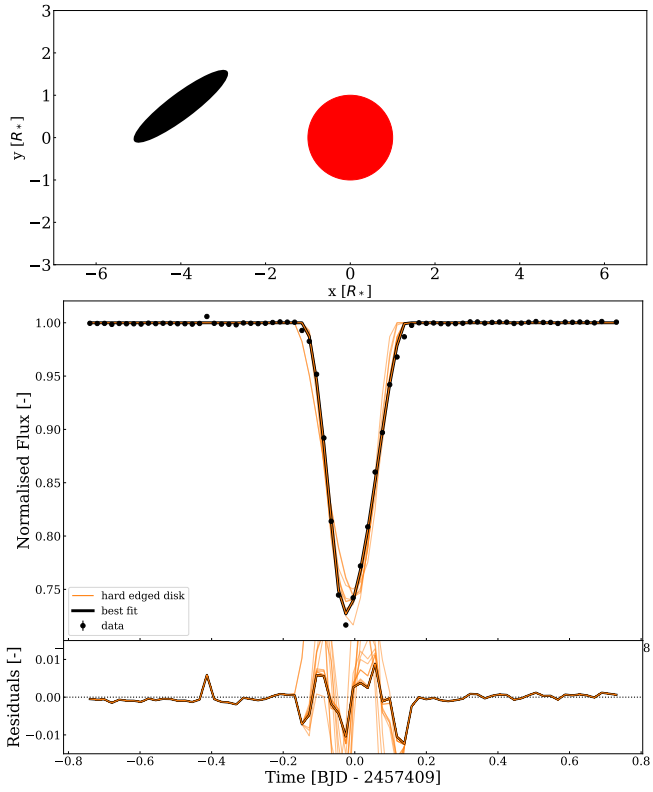

Fig. 5. *Upper*: depiction of the best fit result for the hard edged disk. *Lower*: hard edged disk model fits of 300 random walkers with a burn-in of 500 links.

The extended optimisation was performed with 1000 walkers for 700 links using the priors and parameters described.

The results of the MCMC optimisation model fit and a physical depiction of the model are shown in Fig. 5 and summarised in Table 6. Note that the errors displayed in this table are on the MCMC distribution, and thus do not include any systematic errors in the photometry due to unmodelled astronomical noise sources, such as stellar variation.

The residuals of the fit are at around the 1 percent level. However, it is clear from the systematic deviations of the residuals that the modelled eclipse is not wide enough at the start and end of the eclipse and not deep enough at maximum occultation to follow the measured light curve. This pattern suggests that the disk is not quite large enough and prompts an extension of the hard edged model.

3.3. Soft edged disk

Based on the one percent residuals that we see in the hard edged model, we added an outer ring with variable thickness, t_e, and opacity, τ_e, and centre the prior of the soft edged disk model on the best fit of the hard edged disk model. We set the bounds of τ_e to be between 0 and 1, and those of t_e to be the same as R_d. See also Table 4. The addition of a soft edge would increase the width and depth of the eclipse, but the opacity must be less than 1, otherwise this solution would have been found by the hard edged disk optimisation. We initialised 1000 walkers for 1000 links for the soft edged disk model, using the Gaussian priors summarised in Table 5. The results of the MCMC optimisation model fit and a physical depiction of the model are shown in Fig. 6 and summarised in Table 6.

Table 6. Results of the MCMC optimisation.

Parameters	Hard edged disk	Soft edged disk
R_d [R_*]	1.374 ± 0.002	1.163 ± 0.005
t_e [R_*]	–	0.317 ± 0.005
b [R_*]	0.7397 ± 0.0010	0.7537 ± 0.0011
i [°]	77.01 ± 0.03	75.94 ± 0.03
ϕ [°]	36.81 ± 0.05	38.04 ± 0.07
v_t [R_* day^{-1}]	11.589 ± 0.007	$11.501^{+0.007}_{-0.006}$
v_t [km s^{-1}]	77.45 ± 0.05	76.86 ± 0.04
δt [day]	–0.04083 ± 0.00008	$-0.04040^{+0.00009}_{-0.00008}$
τ [-]	1	1
τ_e [-]	–	$0.499^{+0.008}_{-0.011}$

Notes. Transverse velocity is converted from R_* day^{-1} to km s^{-1} using $R_* = 0.83\ R_\odot$.

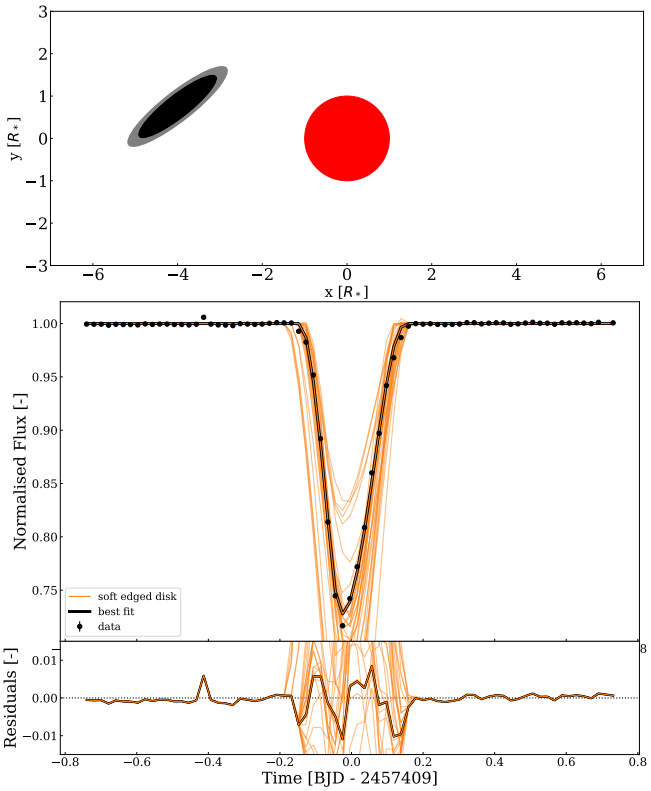

Fig. 6. *Upper*: depiction of the best fit result for the hard edged disk. *Lower*: soft edged disk model fits of 300 random walkers with a burn-in of 550 links.

3.4. Comparison of the two models

The residuals from both models are similar in amplitude and shape, as can be seen in Fig. 7, which overlays the best fits. The soft edged model does give a slightly lower χ^2 value (65 955 for 72 photometric points) compared to the hard edged model (70 729 for 72 photometric points), which implies that the soft edged model is a slightly better fit to the data. However, it is also clear that the addition of a soft edge to the hard edge model was not enough to reduce the observed residuals and thus does not explain their origin.

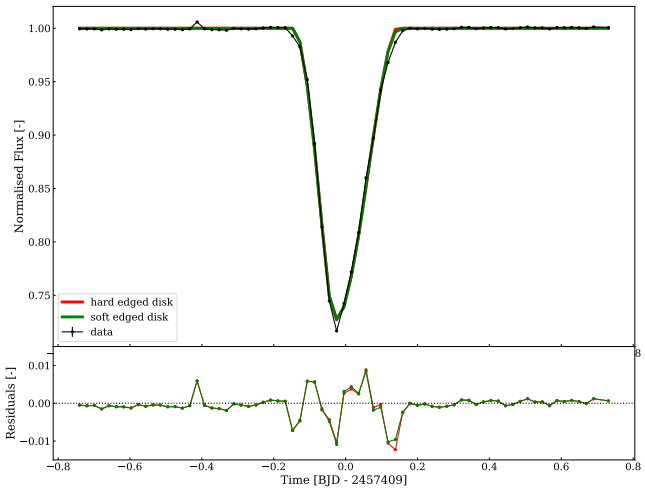

Fig. 7. A comparison of the hard edged model and the soft edged model with residuals.

3.5. Period folding

To search for a plausible orbital period of an occulter orbiting EPIC 2202, we supplemented the data from K2 with data from TESS and several ground-based surveys, as can be seen in Fig. 3.

We folded all the data over a large (60–1800 days) high temporal resolution (step size of 0.001 days) period grid and examined the folded light curve in the region where the K2 eclipse occurs. The routine flags periods where at least three photometric points lie within three times the photometric error of that point from the linearly interpolated K2 data.

The best period candidates were determined by comparing the χ^2 value of folded data with respect to the K2 data ($\chi^2_{\rm model}$) to the χ^2 value of the folded data with respect to a flat line ($\chi^2_{\rm flat}$, i.e. a no eclipse model). The lower the ratio χ^2−ratio = $\chi^2_{\rm flat}/\chi^2_{\rm model}$, the more the folded data follows a no-eclipse scenario. The higher the χ^2−ratio, the more likely the folded data follows an eclipse scenario. A further criterion was that at least one point of the folded data lies in the phase interval where the flux of the K2 data is below a flux of 85%. This is to ensure that the periods investigated actually contain data in the deepest part of the eclipse.

Of all the periods investigated, 13 out of 15 periods with a χ^2−ratio >400 suggest a fundamental period of 290.230 days, and 2 out of 15 periods suggest a fundamental period of 235.587 days (see Table 7 for more details). For a period of 290.230 days, photometry with a χ^2−ratio >400 was found for 2 and 4 times the period, but not for 3 times the period due to incomplete photometric coverage (see Fig. 8). For a period 235.587 days there was no reliable photometry for a multiple of the period, due to incomplete coverage or due to the absence of points in the deepest part of the eclipse (with flux values below 85%).

Note that any of the periods where no photometry was folded into the eclipse cannot be ruled out by this period folding analysis. Therefore, there are many more possible periods for EPIC 2202 that cannot be investigated with the available data.

Considering the most likely shorter orbital periods (see Table 7), we can make predictions for the upcoming eclipses of EPIC 2202. The dates, times, and relation to the observed eclipse for the upcoming four eclipses for each period are listed in Table 8.

Table 7. Reasonable fundamental periods (χ^2−ratio > 400).

Period (day)	$n_{\rm phot}$ (within eclipse)	χ^2−ratio ($\chi^2_{\rm flat}/\chi^2_{\rm model}$)
290.230	4	423.564
235.587	3	410.788

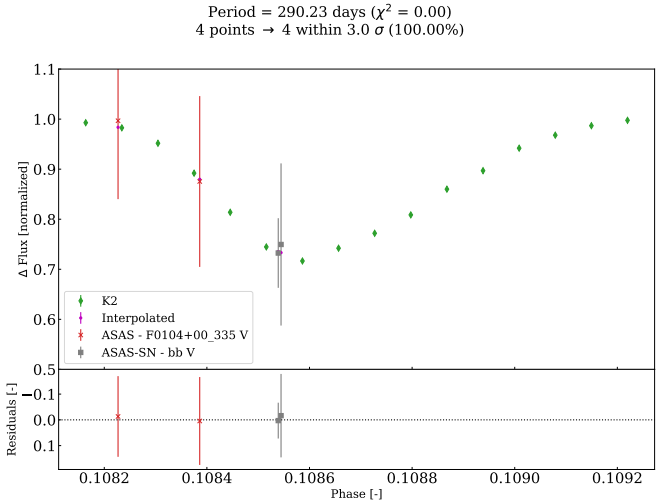

Fig. 8. Phased light curve centred around K2 eclipse with a fold period of 290.230 days.

Table 8. Next transit predictions.

Julian date	Calendar date	UT	Nr. of periods after K2 eclipse
2 459 529.083	10-11-2021	18:47:31	9
2459730.640	31-05-2022	08:09:36	8
2 459 764.670	04-07-2022	08:52:48	10
2 460 000.257	24-02-2023	22:58:05	11
2460020.870	17-03-2023	13:40:48	9
2 460 235.844	18-10-2023	13:03:22	12
2 460 311.100	01-01-2024	19:11:00	10

Notes. Grey rows correspond to $P_{\rm orb}$ = 235.587 days. white rows correspond to $P_{\rm orb}$ = 290.230 days.

3.6. Orbital parameters

We have obtained two transverse velocities from our hard edged and soft edged model, 11.6 and 11.5 R_* day^{-1} respectively, and taking $R_* = 0.83\,R_\odot$ this corresponds to 77.4 and 76.9 km s^{-1}. The eclipse observed by K2 does not repeat within the observation window of K2, which gives us a lower limit on the orbital period, $P_{\rm orb}$. $P_{\rm orb}$ must be larger than the longest time within the K2 data where no eclipse appears, which in this case is 60 days.

If we take the modelled transverse velocity, v_t, and calculate the period of a circular orbit, it results in $P_{\rm orb} \approx 25$ days, which is below the minimum period limit set by the rest of the K2 data, meaning that a circular orbit with this velocity is ruled out. We thus explore eccentric orbits, where we assume that $v_t = v_{\rm peri}$, the velocity at periastron, and create a grid consisting $P_{\rm orb}$, and the mass of the companion, $M_{\rm p}$. We follow the analysis as performed by van Dam et al. (2020) in Sect. 4.4, which we describe shortly here. Using Kepler's Third Law we use $P_{\rm orb}$ to obtain the

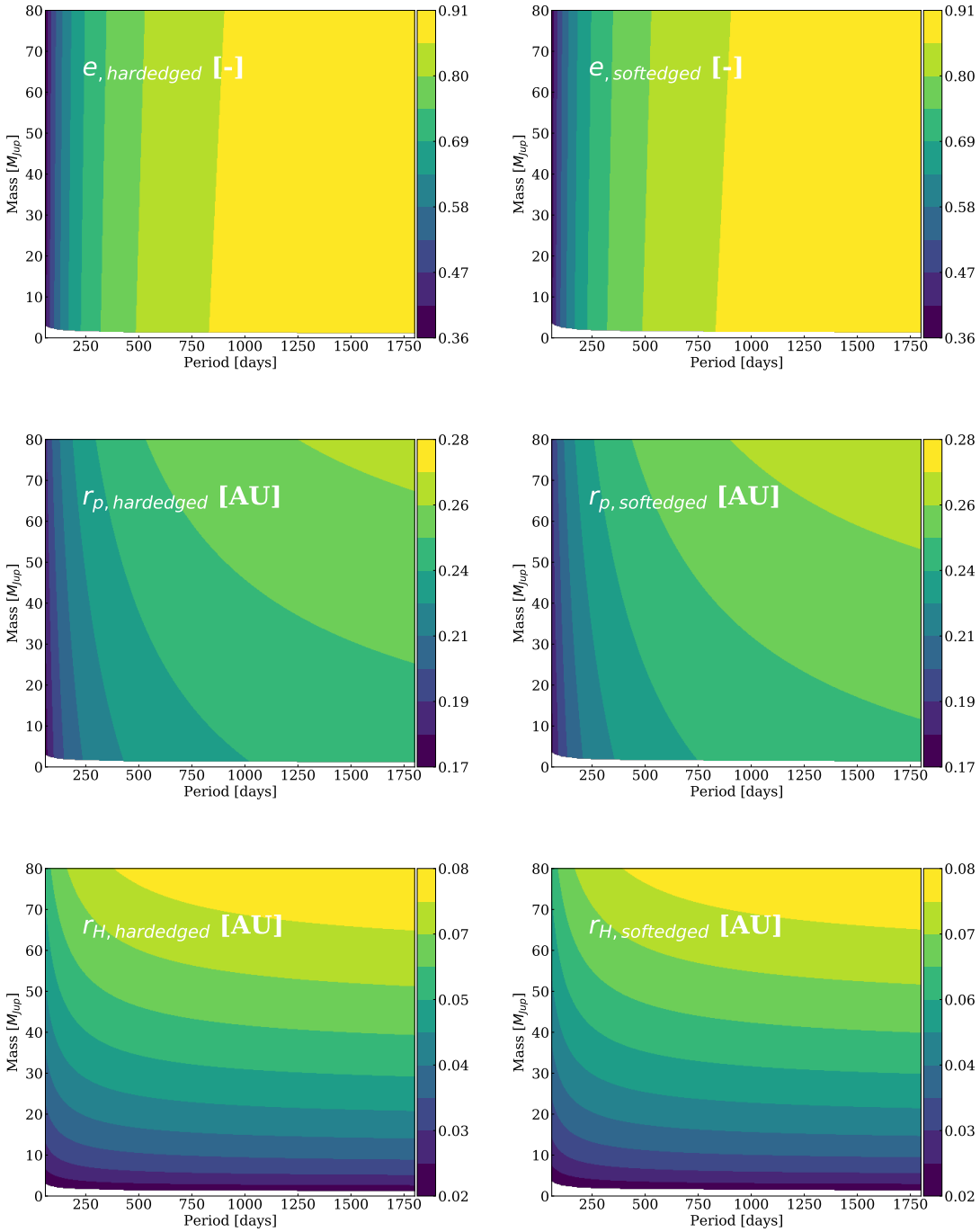

Fig. 9. Parameter space maps for a period between 60 and 1800 days, and mass between 0 and 80 $M_{\rm Jup}$. The *left side* is the hard edged disk, the *right side* is the soft edged disk. The white space at the bottom of the plots is from the constraint $R_{\rm d} < 0.3\ r_{\rm H}$.

semi-major axis, a – when combined with $v_{\rm peri}$ and $M_{\rm p}$, these then determine the eccentricity, e, using the vis-viva equation. Finally as a stability criterion, we state that $M_{\rm p}$ must be large enough that the Hill radius, $R_{\rm Hill}$, of the companion can support the circumsecondary disk ($R_{\rm disk} < 0.3\,R_{\rm Hill}$). We use the same $M_{\rm p}$ bounds from 0–80 $M_{\rm Jup}$, with the upper limit chosen as an inclusive H-burning limit (Saumon & Marley 2008), and a more conservative limit of 73–74 $M_{\rm Jup}$ (Baraffe et al. 2015; Forbes & Loeb 2019). For $P_{\rm orb}$ we set limits of the grid from 60–1800 days, set the upper limit is considered arbitrarily large and is related to the fact that the available photometry does not extend further away from the observed eclipse. The results for the hard edged and soft edged disk models are indistinguishable due to their similar v_t. The parameter space investigation is depicted in Fig. 9 and the orbital parameter ranges at the most likely periods (from Table 7) are presented in Table 9.

The minimum mass is about 1.5 $M_{\rm Jup}$, set by the Hill sphere stability criterion ($R_{\rm disk} < 0.3\,R_{\rm Hill}$) during the periastron passage of the disk. For the most likely period of 290.230 days, the eccentricity of the orbit is around $e = 0.72$, but as can be seen in Fig. 9, the minimum eccentricity for the system can be as low as $e = 0.36$. Longer orbital periods require higher eccentricities in order to keep the velocity at periastron equal to the derived transverse velocity.

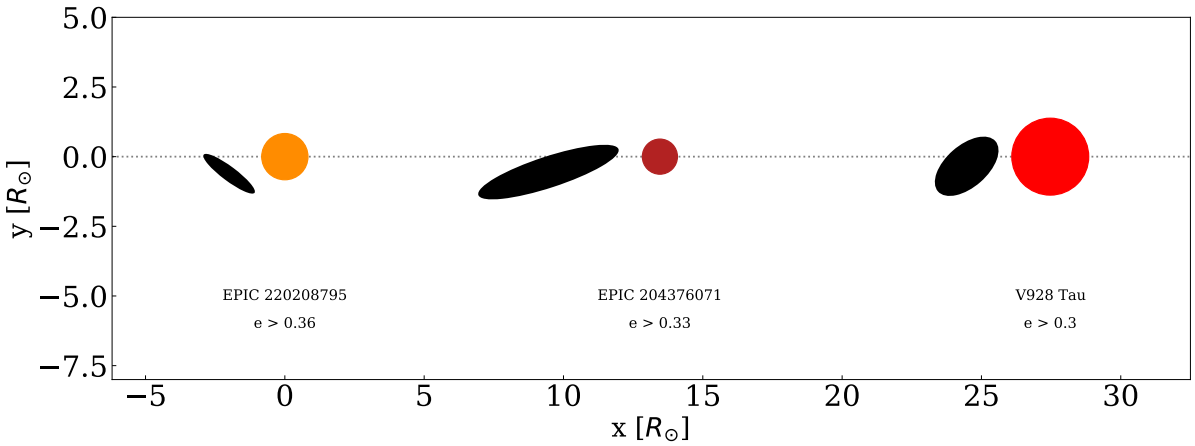

Fig. 10. Comparison of three disk occulters. The disks move from left to right. The colours of the stars are based on their effective temperature relative to each other, where dark red is the coldest, and orange is the hottest star. EPIC 2202 has been mirrored along a line through $y = 0$ compared to the model obtained earlier as this has no effect on the shape of the light curve.

Table 9. Orbital parameters for most likely periods.

Parameter	$P_{\rm orb}$ = 290 days	$P_{\rm orb}$ = 235 days
$r_{\rm ap}$ [AU]	1.40–1.44	1.20–1.21
$r_{\rm peri}$ [AU]	0.22–0.24	0.22–0.23
$r_{\rm H}$ [AU]	0.02–0.07	0.02–0.07
e [-]	0.72–0.73	0.67–0.69

Using the most likely periastron distance we found, and the effective temperature of the star, we can make an estimate of the equilibrium temperature of the disk. For a periastron distance of 0.23 AU, corresponding to a period of about 290.230 days, the equilibrium of a fully absorbing disk around a companion orbiting EPIC 2202 would be about 420 K. Using the second period of 235 days would result in a lower periastron distance, and thus a higher equilibrium temperature, of about 430 K. These temperatures exclude the possibility of a disk made of ice, so we conclude the disk is made of silicates.

4. Discussion

4.1. The EPIC 2202 eclipser

We have found two likely models of disks that could be responsible for the eclipse of EPIC 2202, a fully opaque disk, and an opaque disk with a soft edge. Taking the simpler of the two models, the hard edged model gives a simple template that can be improved upon by adding more degrees of freedom, such as adding scattering or modelling an exponentially thinning disk. We have found a most likely period for the system based on time-series photometry from ground-based surveys, but it does not cover the whole time domain, which, combined with the short duration of the eclipse likely means that we are missing other eclipses that could determine the period of the system.

4.2. A population of small disk occulters

There have been two other cases of circumsecondary disk occulters similar in size to EPIC 2202. The first is a disk around EPIC 2043 (Rappaport et al. 2019b), and the second is a disk around the binary star system V928 Tau (van Dam et al. 2020). A comparison between the radii of these stars as well as the parameters of the disk model obtained can be seen in Table 10, and a comparison of the three systems with disk models can be seen in Fig. 10. Note that for EPIC 2202, Table 10 and Fig. 10 show the simpler hard edged model.

Table 10. Best fit values for the small disk occulter systems.

Parameter	EPIC 2202 [(a)]	EPIC 2043	V928 Tau [(b)]
R_* [$R_\odot$]	0.83	0.63	1.38
$R_{\rm d}$ [R_*]	1.37	4.20	0.99
$R_{\rm d}$ [$R_\odot$]	1.14	2.60	1.39
b [R_*]	–0.74	–0.88	–0.25
i [°]	77.0	77.8	56.8
ϕ [°]	-36.8	18.1	41.2
v_t [km s^{-1}]	77.4	38.0	73.5
Min. e [-]	0.36	0.33	0.30
Min. $r_{\rm peri}$ [AU]	0.17	0.13	0.10

Notes. [(a)]Values from hard edged model. Note that b and ϕ are flipped for easier comparison between the systems. [(b)]Values taken around the primary star.

All of these systems have an inclination, tilt, and non-zero impact parameter, which produces the asymmetric eclipse. Compared to the EPIC 2043 and V928 Tau systems, the companion of EPIC 2202 has the smallest disk in absolute size. Nevertheless, all of these disks are larger than the size expected for Roche rings, where the tidal disruption radius is considerably smaller for the assumed masses. In terms of disk size relative to the star, the disk around EPIC 2202 lies between EPIC 2043 and V928 Tau.

The detection of these systems is biased by the method used to find them - asymmetric eclipses with depths of tens of percent, in stars with flat or slowly varying light curves due to astrophysical activity. If the disks are close to edge on, then their photometric signal may well be very small and therefore undetectable. Having a less than 90° inclination with a tilt between 10° and 70°, and a non-zero impact parameter to break symmetry, results in an asymmetric light curve that can be visually identified. We propose that similar systems are present in the

Kepler and K2 light curves, but they have not been identified as such. Identification of these disks through photometry from the ground is especially challenging, given the typically short duration of these eclipses, on the timescales of hours or less.

All three companions are required to be in an eccentric orbit around the star, with a minimum eccentricity of about 0.3, in order to explain the derived transverse velocity and the lack of other eclipses within the K2 data set. There are of the order of 200 planets detected with eccentricities greater than 0.3, and with orbital periods between 100 and 1000 days[6] so these orbital parameters are not unusual, although higher measured eccentricities are more rare for multiple exoplanet systems (Limbach & Turner 2015). This minimum eccentricity could be explained by a perturbing companion that causes the companion with the inclined disk to be in an eccentric orbit – the V928 Tau system is a binary star system, but we are not currently aware of any companions around EPIC 2043 or EPIC 2202. A peturbing companion may provide an explanation for the disks in the form of a planetessimal collision caused by a strong scattering event that put the companion into the observed eccentricity that we deduce.

All three light curves show a similar pattern of residuals – the points of ingress and egress show deviations from our model leading to the large χ^2 values, and there is a difference in the deepest part of the eclipse, possibly as a result of the model not constraining enough degrees of freedom for an accurate model. Especially in the case of EPIC 2202 and V928 Tau, there is a distinct and similar down-up-down-up-down pattern in the residuals (see Figs. 5–7). For EPIC 2043, the residual pattern starts with a down-up pattern, but afterwards it is less distinct. The down-up-down-up-down pattern comes from the actual eclipse having less steep 'wings' than the model allows for and a deeper minimum. Both for EPIC 2202 and V928 Tau adding a soft edge to the model did not significantly improve the fit. This alludes to a physical phenomenon which is not included in the model. Future studies will include forward scattering and more complex structures for the putative disks.

5. Conclusions

We looked at the light curves initially found in K2 data by LaCourse & Jacobs (2018), from which we selected EPIC 2202 as the most likely candidate of a circumsecondary disk transit. Using a modified version of `pyPplusS` in combination with `emcee`, we modelled the eclipse with a hard edged and soft edged disk. Both of the models have similar residuals that the fitting did not account for. This distinct down-up-down-up-down pattern in the residuals is also seen in the proposed inclined disk system of V928 Tau, and also partly in EPIC 2043. The hard edged model is the simplest of the two, and so we keep our model of an opaque disk around a companion of EPIC 2202, with a disk size of 1.37 R_*, an impact parameter of 0.74 R_*, an inclination of 77.01°, a tilt of 36.81° and a transverse velocity of 77.4 km s^{-1}. A period analysis using ground-based data of EPIC 2202 resulted in two most likely periods, namely, 235.587 and 290.230 days. Taking the fitted transverse velocity we derived orbital parameters of the companion, such as a minimum eccentricity of ~0.36. EPIC 2043 and V928 Tau have roughly the same minimal eccentricity. This eccentricity could be caused by a perturbing companion, but for EPIC 2043 and EPIC 2202 it is not known if there is such a companion.

Future research includes constraining the period of the companion by detecting other eclipses, or by spectroscopic monitoring to determine the mass, or upper limit on the mass, of the secondary companion. The star is an early K dwarf star, which is more amenable to spectroscopic radial velocity measurements, as the other two systems are around M dwarf stars. If we assume that the periastron velocity was observed during the eclipse, we can estimate the amplitude of the radial velocity curve to be of the order of 70 km s^{-1} $(M_P/M_*) \approx 250$ m s^{-1}, which would be possible to observe with a spectrograph on an 8m-class telescope. The eclipse duration is only 7.2 h, which makes it difficult to detect from ground-based observatories subject to diurnal window functions, but using the predictions for next eclipses based on the found periods, there could be observations planned for these dates to constrain the period of the companion. An observational campaign for the American Association of Variable Star Observers (AAVSO) would be a likely path for detecting subsequent eclipses, although the magnitude of EPIC 2202 might leave it as observable for larger aperture telescopes. Direct imaging and high contrast observations of the star could see if there is a perturbing companion around EPIC 2043 or EPIC 2202, as well as observations in filters other than K2's K_p filter. Observations during future eclipses will help determine the specific composition and grain size distribution of the disk and companion. Taking spectra of the star and then comparing its absorption features to the absorption features of the disk could tell us about any chemical reactions taking place in the disk. The model can be extended to include scattering, an exponentially thinning disk or more rings with variable opacity to improve upon the model and find out what the origin is of the pattern in the residuals.

Determining the orbital period of these three systems, and finding more such systems within current and future wide field photometric surveys will give us an idea of their occurrence statistics. Ideally, finding the orbital period of one of these systems will enable a spectroscopic campaign that can characterise the makeup and chemistry within these disks.

Acknowledgements. This research has used the SIMBAD database, operated at CDS, Strasbourg, France (Wenger et al. 2000). This work has used data from the European Space Agency (ESA) mission *Gaia* (`https://www.cosmos.esa.int/gaia`), processed by the *Gaia* Data Processing and Analysis Consortium (DPAC, `https://www.cosmos.esa.int/web/gaia/dpac/consortium`). Funding for the DPAC has been provided by national institutions, in particular the institutions participating in the *Gaia* Multilateral Agreement. To achieve the scientific results presented in this article we made use of the Python programming language (Python Software Foundation, `https://www.python.org/`), especially the SciPy (Virtanen et al. 2020), NumPy (Oliphant 2006), Matplotlib (Hunter 2007), emcee (Foreman-Mackey et al. 2013), and astropy (Astropy Collaboration 2013, 2018) packages. This paper includes data collected by the *Kepler* mission and obtained from the MAST data archive at the Space Telescope Science Institute (STScI). Funding for the *Kepler* mission is provided by the NASA Science Mission Directorate. STScI is operated by the Association of Universities for Research in Astronomy, Inc., under NASA contract NAS 5–26555. We thank the Las Cumbres Observatory and its staff for its continuing support of the ASAS-SN project, and the Ohio State University College of Arts and Sciences Technology Services for helping us set up and maintain the ASAS-SN variable stars and photometry databases. ASAS-SN is supported by the Gordon and Betty Moore Foundation through grant GBMF5490 to the Ohio State University and NSF grant AST-1515927. Development of ASAS-SN has been supported by NSF grant AST-0908816, the Mt. Cuba Astronomical Foundation, the Center for Cosmology and AstroParticle Physics at the Ohio State University, the Chinese Academy of Sciences South America Center for Astronomy (CASSACA), the Villum Foundation, and George Skestos. Part of this research was carried out in part at the Jet Propulsion Laboratory, California Institute of Technology, under a contract with the National Aeronautics and Space Administration (80NM0018D0004). This publication makes use of VOSA, developed under the Spanish Virtual Observatory project supported by the Spanish MINECO through grant AyA2017-84089. VOSA has been partially updated by using funding from

[6] For example, see `https://exoplanetarchive.ipac.caltech.edu/cgi-bin/TblView/nph-tblView?app=ExoTbls&config=PS`

the European Union's Horizon 2020 Research and Innovation Programme, under Grant Agreement number 776403 (EXOPLANETS-A).

References

Adelman-McCarthy, J. K. et al. 2011, VizieR Online Data Catalog: II/306
Aihara, H., Allende Prieto, C., An, D., et al. 2011, ApJS, 193, 29
Alencar, S. H. P., Teixeira, P. S., Guimaraes, M. M., et al. 2010, A&A, 519, A88
Anders, F., Khalatyan, A., Chiappini, C., et al. 2019, A&A, 628, A94
Ansdell, M., Gaidos, E., Rappaport, S. A., et al. 2016, ApJ, 816, 69
Ansdell, M., Gaidos, E., Jacobs, T. L., et al. 2019, MNRAS, 483, 3579
Armitage, P. J. 2011, ARA&A, 49, 195
Astropy Collaboration (Robitaille, T. P., et al.) 2013, A&A, 558, A33
Astropy Collaboration (Price-Whelan, A. M., et al.) 2018, AJ, 156, 123
Bai, Y., Liu, J., Bai, Z., Wang, S., & Fan, D. 2019, AJ, 158, 93
Bailer-Jones, C. A. L., Rybizki, J., Fouesneau, M., Demleitner, M., & Andrae, R. 2021, AJ, 161, 147
Baraffe, I., Homeier, D., Allard, F., & Chabrier, G. 2015, A&A, 577, A42
Bayo, A., Rodrigo, C., Barrado Y Navascués, D., et al. 2008, A&A, 492, 277
Bianchi, L., Herald, J., Efremova, B., et al. 2011, Ap&SS, 335, 161
Bilir, S., Ak, S., Karaali, S., et al. 2008, MNRAS, 384, 1178
Borucki, W. J., Koch, D., Basri, G., et al. 2010, Science, 327, 977
Boyajian, T. S., LaCourse, D. M., Rappaport, S. A., et al. 2016, MNRAS, 457, 3988
Castelli, F., & Kurucz, R. L. 2003, IAU Symp. 210, A20
Cody, A. M., & Hillenbrand, L. A. 2018, AJ, 156, 71
Cody, A. M., Stauffer, J., Baglin, A., et al. 2014, AJ, 147, 82
Cutri, R. M., Skrutskie, M. F., van Dyk, S., et al. 2003, 2MASS All Sky Catalog of point sources (IPAC) (USA: NASA)
Deming, D., Knutson, H., Kammer, J., et al. 2015, ApJ, 805, 132
Eker, Z., Bakış, V., Bilir, S., et al. 2018, MNRAS, 479, 5491
Feinstein, A. D., Montet, B. T., Foreman-Mackey, D., et al. 2019, PASP, 131, 094502
Forbes, J. C., & Loeb, A. 2019, ApJ, 871, 227
Foreman-Mackey, D., Hogg, D. W., Lang, D., & Goodman, J. 2013, PASP, 125, 306
Gaia Collaboration (Brown, A. G. A., et al.) 2018, A&A, 616, A1
Gaia Collaboration (Brown, A. G. A., et al.) 2021, A&A, 649, A1
Gänsicke, B. T., Schreiber, M. R., Toloza, O., et al. 2019, Nature, 576, 61
Handler, G. 2013, in Planets, Stars and Stellar Systems: Stellar Structure and Evolution, eds. T. D. Oswalt, & M. A. Barstow (Dordrecht, The Netherlands: Springer), 4 , 207
Hardegree-Ullman, K. K., Zink, J. K., Christiansen, J. L., et al. 2020, ApJS, 247, 28
Heinze, A. N., Tonry, J. L., Denneau, L., et al. 2018, AJ, 156, 241
Howell, S. B., Sobeck, C., Haas, M., et al. 2014, PASP, 126, 398
Huber, D., Bryson, S. T., Haas, M. R., et al. 2016, ApJS, 224, 2
Hunter, J. D. 2007, Comput. Sci. Eng., 9, 90
Joy, A. H. 1945, ApJ, 102, 168
Kennedy, G. M., Ginski, C., Kenworthy, M. A., et al. 2020, MNRAS, 496, L75
Kenworthy, M. A., & Mamajek, E. E. 2015, ApJ, 800, 126
Kley, W., & Nelson, R. P. 2012, ARA&A, 50, 211
Kochanek, C. S., Shappee, B. J., Stanek, K. Z., et al. 2017, PASP, 129, 104502
LaCourse, D. M., & Jacobs, T. L. 2018, Res. Notes AAS, 2, 28,
Lallement, R., Capitanio, L., Ruiz-Dern, L., et al. 2018, A&A, 616, A132
Lanza, A. F., Bonomo, A. S., & Rodono, M. 2007, A&A, 464, 741
Limbach, M. A., & Turner, E. L. 2015, Proc. Natl. Acade. Sci., 112, 20
Luger, R., Agol, E., Kruse, E., et al. 2016, AJ, 152, 100
Luger, R., Kruse, E., Foreman-Mackey, D., Agol, E., & Saunders, N. 2018, AJ, 156, 99
Mayo, A. W., Vanderburg, A., Latham, D. W., et al. 2018, AJ, 155, 136
McCall, M. L. 2004, AJ, 128, 2144
Minniti, D., Lucas, P., Emerson, J., et al. 2010, New Astron., 15, 433
Minniti, D., Saito, R. K., Forster, F., et al. 2017, ApJ, 849, L23
Olah, K., Kollath, Z., Granzer, T., et al. 2009, A&A, 501, 703
Oliphant, T. E. 2006, A Guide to NumPy (USA: Trelgol Publishing), 1
Pecaut, M. J., & Mamajek, E. E. 2013, ApJS, 208, 9
Pojmanski, G. 1997, Acta Astron., 47, 467
Pojmanski, G. 2005, VizieR Online Data Catalog: 0050, J/other/AcA/50
Rappaport, S., Vanderburg, A., Jacobs, T., et al. 2018, MNRAS, 474, 1453
Rappaport, S., Vanderburg, A., Kristiansen, M. H., et al. 2019a, MNRAS, 488, 2455
Rappaport, S., Zhou, G., Vanderburg, A., et al. 2019b, MNRAS, 485, 2681
Rein, E., & Ofir, A. 2019, VizieR Online Data Catalog: 749
Ricker, G. R., Winn, J. N., Vanderspek, R., et al. 2015, J. Astron. Teles. Instrum. Syst., 1, 014003
Saumon, D., & Marley, M. S. 2008, ApJ, 689, 1327
Schlafly, E. F., & Finkbeiner, D. P. 2011, ApJ, 737, 103
Shappee, B. J., Prieto, J. L., Grupe, D., et al. 2014, ApJ, 788, 48
Simon, J. D., Shappee, B. J., Pojmanski, G., et al. 2018, VizieR Online Data Catalog: J/ApJ/853/77
Sing, D. K. 2010, A&A, 510, A21
Skrutskie, M. F., Cutri, R. M., Stiening, R., et al. 2006, AJ, 131, 1163
Smith, L. C., Koposov, S. E., Lucas, P. W., et al. 2021, MNRAS, 505, 1992
Southworth, J. 2015, Astrophysics Source Code Library [record ascl:1511.016]
Stassun, K. G., Oelkers, R. J., Paegert, M., et al. 2019, AJ, 158, 138
Teachey, A., Kipping, D. M., & Schmitt, A. R. 2017, AJ, 155, 36
Thompson, S. E., Coughlin, J. L., Hoffman, K., et al. 2018, ApJS, 235, 38
Tonry, J. L., Denneau, L., Heinze, A. N., et al. 2018, PASP, 130, 064505
van Dam, D., Kenworthy, M., David, T., et al. 2020, AJ, 160, 285
Vanderburg, A., Johnson, J. A., Rappaport, S., et al. 2015, Nature, 526, 546
van Werkhoven, T. I. M., Kenworthy, M. A., & Mamajek, E. E. 2014, MNRAS, 441, 2845
Virtanen, P., Gommers, R., Oliphant, T. E., et al. 2020, Nat. Methods, 17, 261
Wenger, M., Ochsenbein, F., Egret, D., et al. 2000, A&AS, 143, 9
Williams, J. P., & Cieza, L. A. 2011, ARA&A, 49, 67
Zieba, S., Zwintz, K., Kenworthy, M. A., & Kennedy, G. M. 2019, A&A, 625, L13